

Second 0^+ state of unbound ^{12}O : Scaling of mirror asymmetry

D. Suzuki,^{1,2,3,*} H. Iwasaki,^{4,5,6} D. Beaumel,¹ M. Assié,¹ H. Baba,² Y. Blumenfeld,¹ F. de Oliveira Santos,⁷ N. de Séréville,¹ A. Drouart,⁸ S. Franchoo,¹ J. Gibelin,⁹ A. Gillibert,⁸ S. Giron,¹ S. Grévy,¹⁰ J. Guillot,¹ M. Hackstein,⁶ F. Hammache,¹ N. Keeley,¹¹ V. Lapoux,⁸ F. Maréchal,¹ A. Matta,¹ S. Michimasa,¹² L. Nalpas,⁸ F. Naqvi,⁶ H. Okamura,¹³ H. Otsu,² J. Pancin,⁸ D. Y. Pang,⁷ L. Perrot,¹ C. M. Petrache,¹⁴ E. Pollacco,⁸ A. Ramus,¹ W. Rother,⁶ P. Roussel-Chomaz,⁸ H. Sakurai,^{2,3} J.-A. Scarpaci,¹⁴ O. Sorlin,⁷ P. C. Srivastava,⁷ I. Stefan,¹ C. Stodel,⁷ Y. Tanimura,¹ and S. Terashima²

¹Institut de Physique Nucléaire, CNRS-IN2P3, Université Paris-Sud, Université Paris-Saclay, 91406 Orsay Cedex, France

²RIKEN Nishina Center, 2-1 Hirosawa, Wako, Saitama 351-0198, Japan

³Department of Physics, University of Tokyo, 7-3-1 Hongo, Bunkyo, Tokyo 113-0033, Japan

⁴National Superconducting Cyclotron Laboratory, Michigan State University, East Lansing, Michigan 48824, USA

⁵Department of Physics and Astronomy, Michigan State University, East Lansing, Michigan 48824, USA

⁶Institut für Kernphysik, Universität zu Köln, Zùlpicher Straße 77, 50937 Köln, Germany

⁷GANIL, CEA/DSM - CNRS/IN2P3, Boulevard Henri Becquerel, BP 55027, F-14076 Caen Cedex 5, France

⁸CEA-Saclay, DSM/IRFU SPhN, F-91191 Gif-sur-Yvette Cedex, France

⁹LPC Caen, ENSICAEN, Université de Caen, CNRS/IN2P3 Caen Cedex, France

¹⁰Centre d'Études Nucléaires de Bordeaux Gradignan, Université Bordeaux 1, CNRS/IN2P3, UMR 5797, Chemin du Solarium, BP 120, 33175 Gradignan, France

¹¹National Centre for Nuclear Research, ul. Andrzejka Sołtana 7, 05-400 Otwock, Poland

¹²Center for Nuclear Study, University of Tokyo, RIKEN Campus, 2-1 Hirosawa, Wako, Saitama 351-0198, Japan

¹³RCNP, Osaka University, 10-1 Mihogaoka, Ibaraki 567-0047, Japan

¹⁴CSNSM, CNRS/IN2P3, Université Paris-Sud, UMR8609, F-91405 Orsay-Campus, France

(Received 30 November 2015; published 23 February 2016)

The unbound ^{12}O nucleus was studied via the two-neutron transfer (p,t) reaction in inverse kinematics using a radioactive ^{14}O beam at 51 MeV/u. Excitation energy spectra and differential cross sections were deduced by the missing mass method using MUST2 telescopes. We achieved much higher statistics compared to the previous experiments of ^{12}O , which allowed accurate determination of resonance energy and unambiguous spin and parity assignment. The ^{12}O resonance previously reported using the same reaction was confirmed at an excitation energy of $1.62 \pm 0.03(\text{stat.}) \pm 0.10(\text{syst.})$ MeV and assigned spin and parity of 0^+ from a distorted-wave Born approximation analysis of the differential cross sections. Mirror symmetry of ^{12}O with respect to its neutron-rich partner ^{12}Be is discussed from the energy difference of the second 0^+ states. In addition, from systematics of known 0^+ states, a distinct correlation is revealed between the mirror energy difference and the binding energy after carrying out a scaling with the mass and the charge. We show that the mirror energy difference of the observed 0^+ state of ^{12}O is highly deviated from the systematic trend of deeply bound nuclei and in line with the scaling relation found for weakly bound nuclei with a substantial $2s_{1/2}$ component. The importance of the scaling of mirror asymmetry is discussed in the context of *ab initio* calculations near the drip lines and universality of few-body quantum systems.

DOI: [10.1103/PhysRevC.93.024316](https://doi.org/10.1103/PhysRevC.93.024316)

I. INTRODUCTION

Light nuclei near the drip lines provide unique access to nucleons weakly bound at the Fermi surface. It is widely accepted that these nucleons, when filling orbitals with low angular momenta (L), reach far beyond the classical turning point of a binding potential via tunneling effects, generating various exotic phenomena that are unusual in stable nuclei, such as neutron halos [1,2], coupling to the continuum [3,4], dineutron correlations [5–7], or universal three-body states [8–11].

Experimental data that stress the importance of finite binding effects are accumulating. Recent studies [12,13] presented a unique finding that some observables of weakly

bound states show a simple and smooth evolution as a function of binding energies, as if details of short-range interactions are overshadowed by geometrical effects of finite binding. For instance, Riisager *et al.* revealed that the sizes of halo states are inversely related to the binding energies, and their relation only depends on angular momenta L of valence nucleons after scaling with the reference length and mass [9,12]. Hoffman *et al.* found that energies of $2s_{1/2}$ states relative to $1d_{5/2}$ states smoothly decrease toward the drip line in light nuclei with a neutron number of $N = 5$ to 10. These systematic evolutions point to crucial roles of finite binding in universal scaling of halo state properties [9,12] or in describing major changes in shell structure [13].

Accurate treatment of small L orbitals near thresholds constitutes a major challenge in modern structure calculations [5,6,8–11,14–17]. As these orbitals require much larger coordinate space than others, large-scale calculations based on the

*Corresponding author: daisuke.suzuki@ribf.riken.jp

shell model with residual interactions [18,19] or the *ab initio* approach using realistic nuclear forces [20–23] are rendered highly difficult. Special techniques such as the Gamow shell model using complex eigenstates [15], an effective interaction from the monopole-based-universal interaction in Woods-Saxon bases [16], or the coupled-cluster method [17] have been developed to describe nuclei near and beyond the drip lines. Another group of theories are based on simplified models often assuming a cluster of an inert core and a few valence nucleons for the sake of enabling accurate and explicit treatment of finite potentials [5,6,8–11]. For better treatment and understanding of finite binding effects, it is important to track evolution of physical observables sensitive to these effects toward the drip lines.

In this paper, we report on the level scheme of the unbound and proton-rich ^{12}O nucleus and discuss how weak binding effects characterize the evolution of mirror symmetry breaking. Asymmetry in level energies between mirror nuclei is another observable sensitive to weakly bound orbitals with small L . The asymmetry for $s_{1/2}$ states is well known as the so-called Thomas-Ehrman shift [24,25], in which excitation energies of $s_{1/2}$ states in proton-rich nuclei are much lower than in neutron-rich mirror nuclei. This is due to the unusually lower Coulomb energy of an s -wave proton with a broader wave function that overlaps less with the rest of the nucleus compared to other orbitals with higher angular momenta. This mechanism makes the difference in energies of mirror states, or mirror energy difference, a very sensitive probe of the spatial structure of orbitals with low angular momenta.

Mirror symmetry of ^{12}O , the lightest oxygen nucleus ever found, will be revealing, as it is located beyond the proton drip line and unbound for two-proton emission by 1.638(24) MeV [26]. The 0_2^+ state predicted near 2 MeV [27,28], and thus more unstable than the ground 0^+ state, is of special interest. In the mirror nucleus ^{12}Be , the 0_2^+ state was found at 2.25 MeV by in-beam γ -ray spectroscopy [29,30] and later confirmed by the charge exchange reaction [31]. The valence neutrons of this 0_2^+ state are thought to occupy the $2s_{1/2}$ orbital as well as the $1p$ orbitals [29–31] due to the disappearance of the shell closure at $N = 8$ in ^{12}Be [32,33]. While the ground state of ^{12}O was already observed in the 1970s [34–36], excited states had been elusive ever since, until a resonance was identified at 1.8(4) MeV in our previous study of the $^{14}\text{O}(p,t)^{12}\text{O}$ reaction by the missing mass method [37,38]. Its much lower excitation energy (E_x) compared to $^{14,16}\text{O}$ undoubtedly evidences the disappearance of the shell closure at the proton number $Z = 8$. However, the statistics were still limited and led to a large error of E_x and ambiguity of the spin and parity (J^π), with a tentative assignment of 0^+ or 2^+ . Another observation of a resonance at 1.968(52) MeV later came from the one-neutron knockout reaction of ^{13}O [39]. The statistical quality was not enough to conclude if this corresponds to the 1.8-MeV resonance or another resonance expected nearby [28]. Besides, no J^π information was obtained. These results limited us to examining in detail the symmetry of the level scheme of ^{12}O with respect to ^{12}Be .

In this study, we remeasured the $^{14}\text{O}(p,t)^{12}\text{O}$ reaction accurately to determine the excitation energy and unambiguously assign J^π . This remeasurement, benefiting from data taken

over a longer period of time, achieved higher statistics by almost one order of magnitude than the previous study [37,38], while relying on the same method and nearly the same setup. The missing mass method was used to deduce the excitation energy and the differential cross sections of the reaction. While the detection of recoiling particles is generally challenging in inverse kinematics due to their low energies, the (p,t) reaction with a highly negative Q value presents advantageous laboratory-frame kinematics that recoiling tritons direct at small forward angles with an energy of several tens MeV. This unique feature allows us to enhance luminosity by using a thick cryogenic hydrogen target and to optimize the detection efficiency by covering forward angles with an array of MUST2 telescopes [40].

This paper consists of six sections. Sections II, III, IV, and V describe the experimental setup, the analysis, the results, and the discussion, respectively. The paper will conclude with a summary in Sec. VI.

II. EXPERIMENT

The experiment was performed at the LISE beam line [41] of the Grand Accélérateur National d'Ions Lourds (GANIL). A secondary beam of ^{14}O at 51 MeV/u was produced by the projectile-fragmentation reaction using a $^{16}\text{O}(8^+)$ beam. The primary beam with a typical intensity of 500 e nA was accelerated to 90 MeV/u by a pair of cyclotrons, CSS1 and CSS2, and directed to a rotating beryllium target of 4 mm in thickness. The target was tilted at 44° with respect to the beam axis to optimize the beam purity and intensity, measuring 1.1 g/cm^2 in an average effective thickness. Fragments thus produced were collected and purified by the LISE spectrometer equipped with a 0.5-mm-thick wedge-shaped degrader of beryllium at the dispersive focal plane. To further improve the purity of ^{14}O , a Wien filter was operated at 150 kV dc at the beginning of the measurement. The recorded data roughly account for one third of the total. The remaining data were taken without using the Wien filter.

The secondary beam was bombarded on a cryogenic hydrogen target [42] at the final focal plane of LISE (Fig. 1).

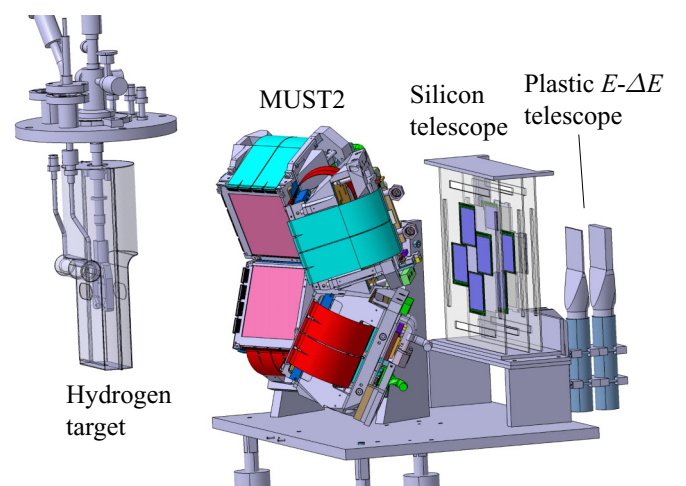


FIG. 1. Schematic drawing of the experimental setup.

The target was installed in a cylindrical vacuum chamber, referred to as M2C, measuring 1 m both in height and in diameter. The target cell had a circular opening of 1 cm in diameter, which was covered by a pair of Mylar foils having an areal density of 0.8 mg/cm^2 each. Another pair of the same Mylar foils sandwiched this opening to create volumes for helium gas, which pressurizes the inner volume to ensure homogeneity of the growing slab of solid hydrogen inside. The designed thickness of solid hydrogen was 1 mm, which corresponds to an areal density of 7.1 mg/cm^2 for the nominal density.

The position and time of beam particles were measured by a pair of multiwire proportional chambers, CATS [43], installed 45 cm and 109 cm upstream of the target, respectively. Each detector has a layer of multiple anode wires sandwiched by two Mylar foils with aluminum electrodes. These cathode electrodes have a square surface of $7 \times 7 \text{ cm}^2$ segmented into 28 strips along the horizontal or the vertical to locate the centroid of image charges, or the impact point of beam particles. To confirm the alignment, calibration measurements were carried out using metallic plates with a series of holes as a position reference. The plate installed 14 cm upstream of each CATS has 1- or 2-mm-diameter holes every 2.5 mm, which serve to collimate the beam into multiple rays and cast a patterned beam image onto the CATS. The holes were reconstructed to the precision of $\pm 0.5 \text{ mm}$. The plates were retracted from the beam line after the calibration run. The time of anode wire signals was recorded by a time-to-analog converter using radio-frequency pulses from CSS2 as the stop signal. The recorded time represents the time of flight (TOF) for beam particles to travel the length of the LISE beam line. The detection efficiency was about 90% each. The intensity of the secondary beams ranged from 1.0×10^5 to 3.0×10^5 particles per second (pps) over the course of the experiment, while that of ^{14}O from 0.7×10^5 to 2.5×10^5 pps.

All the other detectors were installed inside the M2C chamber (Fig. 1). The detector setup was almost the same as the previous experiment except a newly-added plastic telescope. Recoiling tritons were detected by an array of four MUST2 telescopes about 30 cm downstream of the target, each having a $10 \times 10 \text{ cm}^2$ double-sided silicon strip detector (DSSD) followed by a CsI scintillator with 4×4 -fold segments. The detection efficiency reaches about 80% from 10° to 20° in the laboratory frame, and gradually decreases to zero toward 5° and 30° . The DSSDs and the CsI scintillators have thicknesses of $300 \mu\text{m}$ and 4 cm, respectively, enabling energy loss (ΔE) and residual energy (E) measurements. The readout electrode of each side of the DSSDs is segmented into 128 strips to locate the impact position of incident particles.

Scattered particles and their decay products were detected by an array of silicon detectors and a plastic scintillator telescope, both developed at RIKEN. The former was located 55 cm downstream of the target and the latter at 77 cm. The plastic telescope provides coverage at far forward angles from 0° to 1.6° in the laboratory, while the silicon telescope covers larger angles. The silicon telescope consists of three detector layers. Each of the first two layers, 3.4 cm apart along the beam axis, has four $325\text{-}\mu\text{m}$ -thick silicon detectors (labeled $\Delta E1$ and $\Delta E2$), while the third one 1.7 cm downstream of the $\Delta E2$

layer has four 2-mm-thick Si(Li) detectors ($E3$). Each detector has a square pad shape without segmentation and is mounted in an L-shaped insulator support. This design was chosen so that the four detectors can be placed in the windmill arrangement around the beam axis to surround a square hole of $3 \times 3 \text{ cm}^2$. The frameless sides of the detectors are arranged at the nearest side of the beam axis to limit the efficiency loss. The $3 \times 3 \text{ cm}^2$ space is meant to let through the high flux secondary beam and protect the silicon detectors from irradiation damages. This telescope is based on the construction adopted in the previous experiment, but with a few minor updates. First, the hole was narrowed from $4 \times 4 \text{ cm}^2$ to cover more forward angles. Another change is the $\Delta E2$ layer. In the previous study, 2-mm-thick Si(Li) detectors were used for $\Delta E2$ as well as $E3$. However, some $E3$ detectors suffered severe nonuniformity and failed to differentiate the mass number. In this study, we furnished the $E3$ layer with Si(Li) detectors that had properly functioned in the previous study. The $\Delta E2$ layer was equipped with thinner Si detectors. A 1.5-mm-thick aluminum degrader was installed between the $\Delta E1$ and $\Delta E2$ layers to stop ^{10}C particles in the $E3$ layer.

The plastic telescope consists of a stack of two NE102 plastic scintillators 4 cm apart. A 2-mm-thick ΔE counter is followed by a 10-mm-thick E counter, both having the same surface area of $6 \times 6 \text{ cm}^2$. To read out scintillation light, each scintillator is coupled to a photomultiplier tube (PMT) assembly, model H7415, manufactured by Hamamatsu Photonics. Power supply booster circuits are implemented in these PMT assemblies to limit the attenuation of signals at high counting rates.

Signals from the four MUST2 telescopes were fed to MUFEE front-end boards [44] for pulse shaping and then multiplexed to a VXI-standard MUVI digitizer [44]. The other devices were recorded by 14-bit VXI-standard multipurpose digital converters developed by GANIL. The signal processing of the CATS detectors is described in Ref. [43]. Preamplifier signals of the silicon telescope were fed to an amplifier, model N568B manufactured by CAEN, while PMT output signals of the plastic telescope were recorded directly by a 14-bit digital converter operating in the QDC mode. The trigger generation required at least one DSSD strip to be fired in the whole MUST2 array. The energy thresholds of the DSSDs were set to about 0.5 MeV in the MUFEE boards. To monitor beam and scattered particles without bias from the MUST2 telescopes, logic signals of the CATS and the plastic telescope were added to the trigger after prescaling down by a factor of 10^4 . The data acquisition rate was typically 500 Hz with a live time ratio of 80%.

III. ANALYSIS

Beam particles were identified using the time of anode signals of the downstream CATS with respect to RF pulses ($T_{\text{CATS-RF}}$). Shown in Fig. 2(a) is a scatter plot of the energy loss in the plastic ΔE counter (ΔE_{plast}) against $T_{\text{CATS-RF}}$ taken without operating the Wien filter. Prescaled events recorded by the CATS trigger were used. Three distinct clusters correspond to ^{14}O and isotope contaminants ^{12}C and ^{13}N as labeled. Note that the time of ^{12}C is shifted by $+76 \text{ ns}$, which corresponds

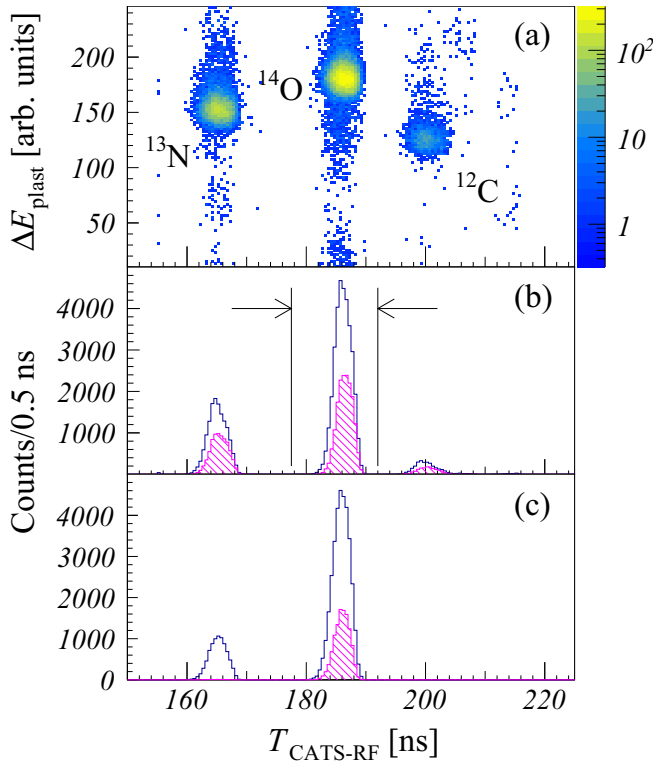


FIG. 2. Identification of the secondary beam. (a) Scatter plot of ΔE_{plast} vs $T_{\text{CATS-RF}}$. $T_{\text{CATS-RF}}$ spectra (b) without and (c) with turning on the Wien filter. The shaded spectra are gated by a 10-mm-diameter cut to the beam spot on the target. The arrows denote the gate to select ^{14}O particles.

to the time interval of RF pulses. This is because ^{12}C particles that arrive later due to a longer TOF do not share RF pulses of the same bunch as ^{14}O and ^{13}N . These clusters are well separated in time as seen in the blank histogram in Fig. 2(b). To select ^{14}O particles, a gate was set on $T_{\text{CATS-RF}}$ as indicated by the arrows. Figure 2(c) shows the same spectrum, but taken with the Wien filter operated at 150 kV dc. It is seen that the purity of ^{14}O is improved with the use of the Wien filter.

Trajectories of beam particles were reconstructed using the hit position information from the pair of CATS detectors. The position of beam particles on the target was obtained by extrapolation. The spot size of the ^{14}O beam was measured to be 4 mm and 1.5 mm RMS in the horizontal and vertical directions, respectively. The spot was 3.5 mm left and 1 mm high relative to the beam axis when viewed from upstream of the target. A 10-mm-diameter cut was set around the beam axis to define the opening of the target and eliminate scattering off the target cell and the heat shield. The rate of ^{14}O particles accepted by this cut varied from 3×10^4 to 8×10^4 pps during the experiment, while the purity stayed at about 65% without the Wien filter and nearly 100% with the filter. This is visualized by the shaded histograms in Figs. 2(b) and 2(c), respectively, that are gated by the circular cut on the beam spot. The total number of ^{14}O particles used in the analysis was 1.4×10^{10} , nearly one order of magnitude higher than that of the previous measurement (1.6×10^9) [37,38].

The impact point on the MUST2 telescopes was located from the position of hit strips on the front and back sides of a DSSD. The scattering angle in the laboratory frame (θ_{lab}) was deduced from this information combined with the angle and position of the beam particle at the target. The DSSDs were calibrated by a standard source containing three different α emitters of ^{239}Pu , ^{241}Am , and ^{244}Cm . The typical resolution was about 50 keV FWHM. The energy calibration of CsI was made by analyzing the E - ΔE correlation between the residual energy in CsI and the energy loss in DSSD. CsI energies in analog-to-digital converter (ADC) counts ($E_{\text{CsI}}^{\text{ADC}}$) were calibrated with respect to residual energies calculated by the SRIM code [45] using calibrated DSSD energies (E_{DSSD}) and lengths traveled by ions in DSSD at given impact angles. However, this method based on the $E_{\text{CsI}}^{\text{ADC}}-E_{\text{DSSD}}$ correlation loses accuracy when E_{DSSD} becomes small and causes large uncertainty in predicted residual energies. In the present reaction, the energy deposition in 300- μm -thick silicon is only 1 MeV or less for recoiling tritons with energies higher than 70 MeV. This constituted the major source of error for E_x in the previous measurement (± 0.4 MeV) [37,38]. In this analysis, the energy calibration was fine-tuned by reconstructing reaction kinematics. We used the data of the $^{14}\text{O}(p,t)^{12}\text{O}$ reaction and the $^{16}\text{O}(p,t)^{14}\text{O}$ reaction, the latter of which was measured as a reference at 39 MeV/u in separate runs during the beam time. We introduced a one-dimensional adjustment function, $E_{\text{CsI}} = c_0 + c_1 E_{\text{CsI}}^{(0)}$, where $E_{\text{CsI}}^{(0)}$ denotes the CsI energy calibrated by the $E_{\text{CsI}}^{\text{ADC}}-E_{\text{DSSD}}$ correlation. The c_0 and c_1 parameters were optimized so that the ground state energies of ^{12}O and ^{14}O are best reproduced after the reconstruction of the (p,t) reactions. The mass excesses were taken from the latest compilation [26]. The high statistical quality of the present data enabled us to apply this method to each crystal segment. A much improved systematic error of $E_x = \pm 0.1$ MeV was estimated from the reconstructed excitation energies of the ^{14}O 2_1^+ state at 7.7 MeV, that was not taken into account in the tuning of c_0 and c_1 . The total kinetic energy (TKE) was deduced by summing E_{DSSD} and E_{CsI} after correcting for the energy deposition in the solid hydrogen target and its window foils. The reaction vertex was assumed at the middle of the target.

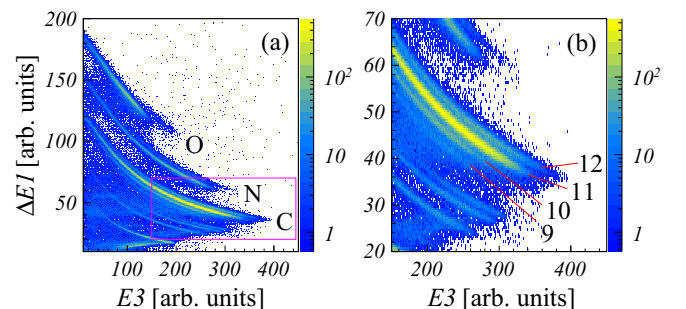


FIG. 3. Identification of scattered particles by the silicon telescope. (a) Scatter plot of $\Delta E1$ vs $E3$ and (b) a magnified view of the enclosed area around the carbon isotopes. The numerical labels denote the mass numbers.

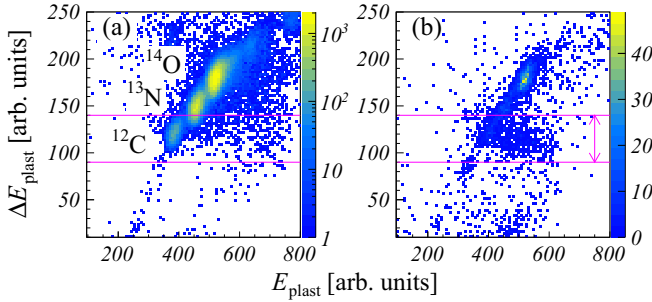


FIG. 4. Identification of scattered particles by the plastic E - ΔE telescope. (a) Scatter plot of ΔE_{plast} vs E_{plast} for the prescaled data recorded by the plastic trigger. (b) The same plot for events with a ^{14}O beam particle and a triton in coincidence. The cut for $Z = 6$ is indicated by the arrow.

^{10}C particles following the $2p$ emission decay of ^{12}O were identified by the E - ΔE method using the silicon and plastic telescopes. The scatter plot of $E3$ vs $\Delta E1$ from the silicon telescope is shown in Fig. 3(a). The area around the loci of carbon isotopes is magnified in Fig. 3(b). The locus for ^{10}C is separated by about 4σ from those of $^{9,11}\text{C}$. The plastic telescope was used to select the atomic number only. During the experiment, both ΔE and E counters experienced a gain shift and a worsening in energy resolution. This should be due to the damages after irradiation of the secondary beam at a rate of about 10^5 pps. The gain shift was corrected for in the analysis software. The degraded energy resolutions still allow us to differentiate the atomic number. A scatter plot of the energy loss ΔE_{plast} against the residual energy in the E counter (E_{plast}) is shown in Fig. 4(a). The prescaled data taken by the plastic trigger were used. It is compared to the same ΔE_{plast} vs E_{plast} plot in Fig. 4(b) obtained from the physics data gated by a ^{14}O beam particle in coincidence with a triton in the MUST2 array. The clusters of ^{14}O , ^{13}N , and ^{12}C beams in plot (a) guide us to identify a cluster of carbon nuclei in plot (b) for scattering data. ^{10}C particles are included in the carbon cluster, but the mass number cannot be differentiated due to the limits of energy resolutions. The cut for $Z = 6$ was thus defined by selecting this cluster with ΔE_{plast} as indicated by the arrow.

IV. RESULTS

The scatter plot of TKE vs θ_{lab} for the $^{14}\text{O}(p,t)$ reaction is shown in Fig. 5(a). A locus visible in the figure agrees with the relativistic reaction kinematics for the ^{12}O ground state. The excitation energy E_x and the center-of-mass scattering angle $\theta_{\text{c.m.}}$ of ^{12}O were deduced from the TKE and θ_{lab} . The angle-integrated spectrum over 10° to 80° is shown by the blank histogram in Fig. 5(b). In addition to the ground state, another narrow peak is distinct near 1.6 MeV as indicated by an arrow. This confirms the resonance at 1.8(4) MeV reported in our previous reports [37,38] with much better statistics.

To measure the background, data were taken without filling the cryogenic target cell. The cell was kept at the operating temperature not to release impurities built on the window foils.

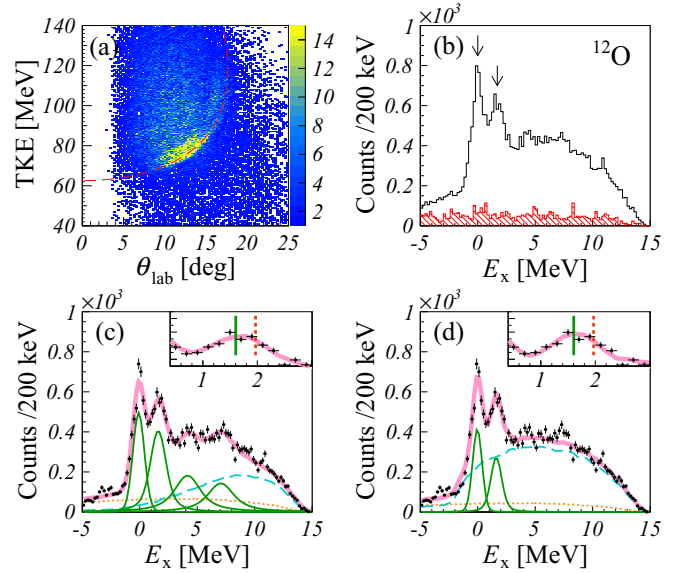


FIG. 5. (a) TKE vs θ_{lab} of recoiling tritons from the $^{14}\text{O}(p,t)^{12}\text{O}$ reaction at 51 MeV/u. The dashed line denotes the theoretical kinematics for the ground state. (b) Angle-integrated excitation energy spectra of ^{12}O . The shaded histogram shows the spectrum taken with an empty target cell. (c) Angle-integrated excitation energy spectrum of ^{12}O after subtracting the empty target cell data. The best fit curve is shown by the thick solid line. The fitting function consists of Voigt functions for ^{12}O resonances (solid green lines) and simulated backgrounds for the direct breakup reactions to ^{10}C , $2p$, and t (dashed blue line) and to ^{11}C , $2p$, and d (dotted orange line). The inset magnifies the region around the excited state. The center of the Voigt function (solid line) is compared to $E_x = 1.968$ MeV (dashed line), the resonance energy reported in Ref. [39]. (d) The same spectrum as (c), but for the fitting function assuming a sequential process for the breakup to ^{10}C , $2p$, and t (dashed blue line).

The resulting spectrum is shown by the shaded histogram in Fig. 5(b) after scaling by the total beam counts. The measured background has a flat distribution and much lower magnitude compared to the data with hydrogen. This ensures that the observed resonances originate in interactions with solid hydrogen.

After subtracting the data of the empty target cell, the excitation energy spectrum was analyzed to deduce the resonance energies and widths (Γ). Contributions from the breakup reactions of ^{14}O were taken into account. Two types of processes were considered for the breakup to ^{10}C , $2p$, and a triton. The first type is that a ^{14}O beam particle directly breaks to the final state without any intermediate states (hereafter referred to as direct breakup). The second proceeds with an intermediate state that consists of p , t , and ^{11}N which promptly decays into ^{10}C and p (sequential breakup). The fitting function also includes another breakup process to $^{11}\text{C} + 2p + d$ that can be mixed into the spectra when ^{11}C and a deuteron are falsely identified as ^{10}C and t . ^{10}C is inevitably misidentified as the plastic telescope only provides Z . Response functions for these backgrounds were simulated by a Monte Carlo simulation code based on the GEANT4 [46] library, where events were generated evenly over

the phase space. A Voigt function [47], a convolution of a Breit-Wigner function with a Gaussian function, was used to fit an ^{12}O resonance. The Breit-Wigner function represents the resonance profile and the Gaussian function the detector response. A common Gaussian width was assumed for all resonances at a given angular bin. The Γ for the ground state was fixed to 72 keV, the upper limit reported in Ref. [39].

The best fit curves are shown in Figs. 5(c) and 5(d), respectively, for the direct and sequential breakup backgrounds. The sequential breakup background largely reproduces the broad bump dominating the experimental spectrum at higher energies. On the other hand, the fitting with the direct breakup background requires the introduction of at least two additional resonances. The best fit leads to one resonance centered at 4.2 MeV and the other at 7.0 MeV, both with $\Gamma = 2.2$ MeV. The fitting curve reproduces minor rises of the spectrum at these energies, which implies that these resonances could be true. However, the statistical significance of these minor peaks is not as high as the ground state or the state at 1.6 MeV. It is also difficult to identify distinct peaks consistently over angles in the angle-gated spectra shown in Figs. 6. We hence consider that these resonances are only suggestive. Regardless of the breakup types, the E_x of the excited state is 1.61(3) MeV from the fits. The Γ is deduced to be 0.83(35) MeV with the direct breakup and 0.38(6) MeV with the sequential breakup. Here the cited errors are statistical.

In our previous study [37,38], the observed resonance is assigned J^π of 0^+ or 2^+ . While a singlet was assumed given statistical uncertainties, this resonance could be a doublet of a 0^+ and a 2^+ state that are expected near 2 MeV from a theoretical prediction [28] as well as the level scheme of ^{12}Be (0_2^+ at 2.25 MeV [29,30] and 2^+ at 2.10 MeV [32,48]), as pointed out in Ref. [28]. In the present spectra with higher statistics, multiple peaks are still not visible near 1.6 MeV. These possible states could, however, be unresolved within the energy resolution of about 0.4 MeV RMS. We hence carefully deduced E_x and Γ by taking the possible doublet into account. In Fig. 7(a), the angular dependence of the yields of the 1.6-MeV peak is shown. This type of presentation, without correcting for experimental conditions, is not common, but is visually helpful to find which ΔL component governs the experimental yields. Note that an angle-gated spectrum was made every 5° with an angular bin of 10° to take more data points, while retaining enough statistics. In Fig. 7(a), it is seen that the yields of the 1.6-MeV resonance concentrate in a peak at 35° . To find ΔL primarily responsible for this distribution, we carried out distorted-wave Born approximation (DWBA) calculations with $\Delta L = 0$ and 2. The details of the DWBA calculations will be described later. The calculated differential cross sections were translated into yields by taking into account the solid angle and the detection efficiency calculated by the GEANT4 simulation. The calculated yields were scaled by a common factor to fit the result of $\Delta L = 0$ to the experimental data. As seen in the figure, the calculated distribution for $\Delta L = 0$ nicely reproduces the peak of yields. In contrast, the distribution of $\Delta L = 2$ is too flat to account for the enhancement of yields from 20° to 50° , indicating that its contribution, if any, is minor. A 0^+ resonance populated with $\Delta L = 0$ is the major component of the peak observed at 1.6 MeV.

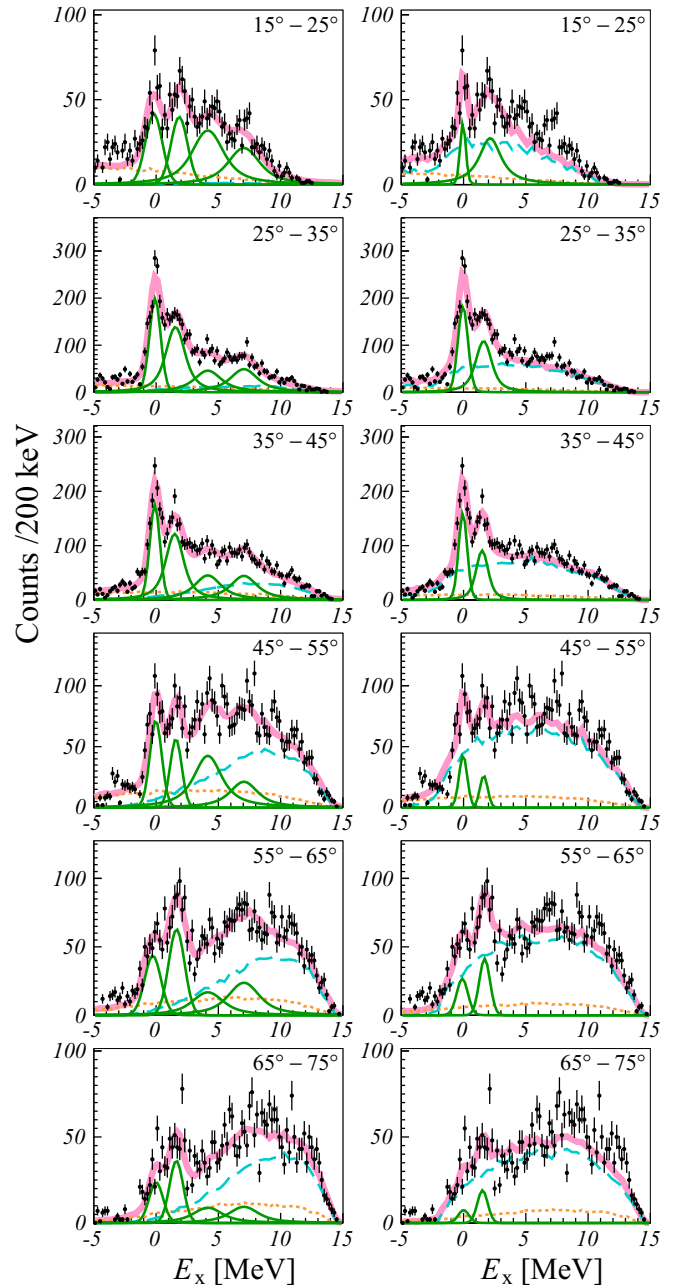


FIG. 6. Angle-gated spectra of ^{12}O . The chosen range of $\theta_{c.m.}$ is shown in each spectrum. The notations are the same as in Fig. 5. The spectra in the left column were analyzed using the direct breakup background, while those in the right column used the sequential breakup background.

If a 2^+ level is mixed into the 1.6-MeV resonance, its contribution is relatively significant at $\theta_{c.m.} < 20^\circ$ or $\theta_{c.m.} > 50^\circ$, where the yields of the 0_2^+ state are low. The mixing may shift E_x and Γ closer to those of the possible 2^+ level at these angles. In the E_x vs $\theta_{c.m.}$ plot of Fig. 7(b), the peak energies stay around 1.6 MeV from 20° to 50° and increase up to 2 MeV at smaller and larger angles. A similar trend is also seen in the Γ values plotted in Fig. 7(c) that are around 1 MeV from 25° to 45° and decrease to zero outside. We

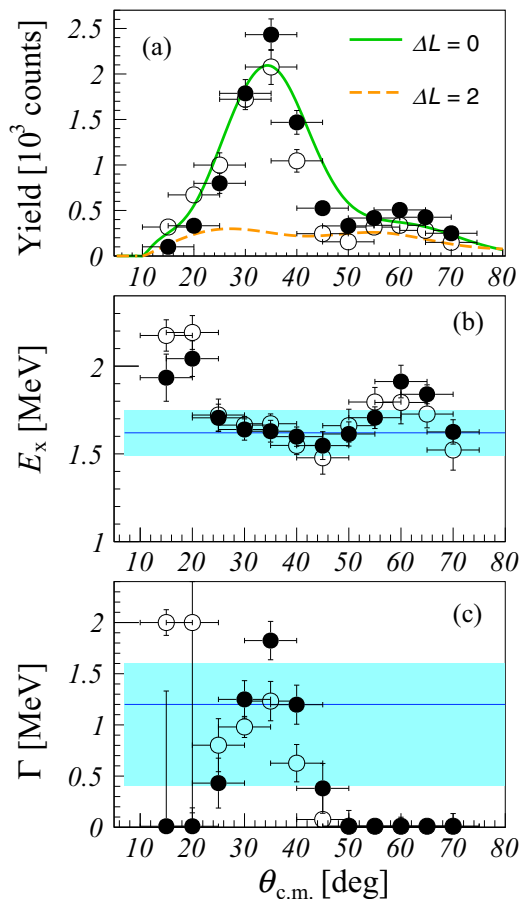


FIG. 7. Angular dependence of (a) yields, (b) E_x , and (c) Γ of the 1.6-MeV resonance in the center of mass. The fitting results using the direct (filled circles) and sequential breakup backgrounds (open circles) are shown. The horizontal bars denote the size of angular bins. The adopted values (blue lines) and their errors (shaded areas) are also displayed. The statistical and systematic errors are added.

cannot, however, rule out the possibility that these are due to experimental uncertainties, as the signal-to-background ratio is much smaller at these angles compared to $\theta_{c.m.} = 20^\circ$ to 50° . The variation of E_x is mostly within the systematic error of ± 0.1 MeV except for a few angular bins. Γ is particularly sensitive to the level of statistics since the excitation energy resolution of about 1 MeV FWHM is comparable to the peak width. More precise measurements will be necessary to differentiate possibly mixed levels.

Reliably to determine the E_x and Γ of the 0^+ resonance, we take the average of these values over $\theta_{c.m.} = 25^\circ$ to 45° , where the contribution of $\Delta L = 0$ dominates regardless of mixing of a 2^+ resonance. The values thus adopted are $1.62 \pm 0.03(\text{stat.}) \pm 0.10(\text{syst.})$ MeV for E_x and $1.2 \pm 0.1(\text{stat.})_{-0.7}^{+0.3}(\text{syst.})$ MeV for Γ , as indicated in Figs. 7(b) and 7(c), respectively. We adopted a conservative systematic error for Γ given its strong variation. The deduced E_x is consistent with our previous value of 1.8(4) MeV [37,38], but lower than 1.986(52) MeV reported in the recent study of the $1n$ knockout reaction at Texas A&M [39]. The difference is visualized in the insets of Figs. 5(c) and 5(d). In Ref. [39],

the question as to whether their resonance is a singlet or a doublet is left open due to statistical uncertainties. As one possible scenario, two different states are observed in the present and knockout [39] experiments. The relative weight of the 0^+ state and an unidentified 2^+ state would differ in the knockout reaction due to reaction mechanisms and/or acceptance, resulting in energy shift.

Differential cross sections were deduced from the yields obtained by fitting the angle-gated spectra (Figs. 6). The detection efficiency simulated by the GEANT4 code and the total beam counts obtained from CATS were used. The thickness of the solid hydrogen target was adjusted to reproduce the absolute cross sections of the reference data of the $^{16}\text{O}(p,t)$ reaction at 39 MeV/u [37,38]. The adopted areal density was 10 mg/cm^2 , which is 10% higher than the reported value of $8.85(17) \text{ mg/cm}^2$ [43]. The differential cross sections thus deduced are shown in Figs. 8 for the two types of breakup backgrounds. The vertical error bars in these figures are statistical. The systematic errors arise from the target thickness estimate (20%) and the detection efficiency simulation (15%). The diffractive patterns of the ground state and the excited state at 1.6 MeV, both characterized by a peak near 30° , well agree with the previous data [37,38] shown in Figs. 8. On the other hand, the absolute cross sections of the 1.6-MeV state differ by a factor of 2 depending on the choice of breakup processes. Since the peak is closer to the high energy bump as seen in Figs. 5(c) and 5(d), its area is sensitive to the shape of the breakup backgrounds.

These results are compared to DWBA calculations. The calculations were similar to those carried out previously for the same system [37,38] with the exception that the $2n$ overlap functions for both heavy and light systems were calculated in a more realistic manner. The $(t|p + 2n)$ overlap was generated according to the prescription of Thompson [51], making the simplifying assumption of a pure s^2 configuration for the triton wave function. The $(^{14}\text{O}|^{12}\text{O} + 2n)$ overlaps were calculated following the procedure of Ref. [52]. Pickup of neutron pairs in the following configurations was assumed for transfers leading to the ground state and the 1.6-MeV excited state of ^{12}O : $(1p_{3/2})^2$, $(1p_{3/2}, 1d_{5/2})$, and $(1p_{3/2}, 1p_{1/2})$ for spin-parity 0^+ , 1^- , and 2^+ , respectively. For pickup leading to the states at 4 and 7 MeV the following configurations were assumed: $(1d_{5/2})^2$, $(1p_{3/2}, 1d_{5/2})$, and $(1d_{5/2}, 2s_{1/2})$ for spin-parity 0^+ , 1^- , and 2^+ , respectively. Other configurations such as $(2s_{1/2})^2$ for 0^+ or $(1p_{3/2}, 2s_{1/2})$ for 1^- were also considered for the states at 4 and 7 MeV, respectively, and confirmed to give almost the same shape of angular distributions. All calculations were performed with the code FRESKO [53] using prior form finite-range DWBA. Entrance and exit channel optical potentials employed the global parameters of Refs. [54] and [55], respectively.

The calculated differential cross sections are scaled to the experimental data in Figs. 8. The DWBA angular distributions with $\Delta L = 0$ well reproduce the experimental data of both ground and 1.6-MeV states. The scaling factors of $\Delta L = 0$ are almost unity for the ground state. This indicates that absolute cross sections of the present reaction calculations are rather reasonable. In the case of the 1.6-MeV state, the scaling factor of $\Delta L = 0$ is also nearly unity for the results using

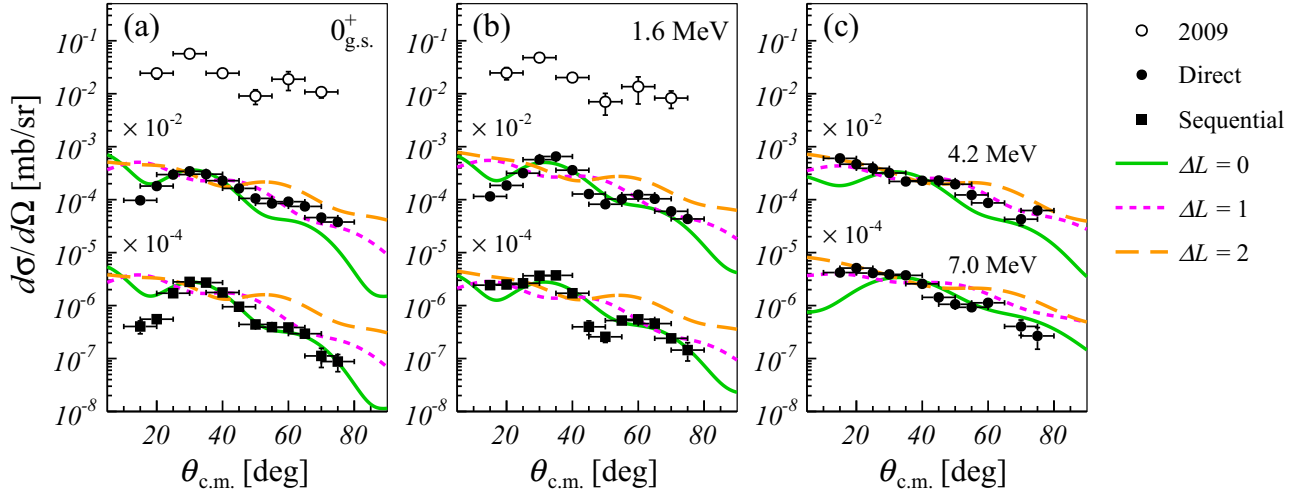


FIG. 8. Differential cross sections of the $^{14}\text{O}(p,t)^{12}\text{O}$ reaction at 51 MeV/u. The experimental data for (a) the ground 0^+ state, (b) the excited state at 1.6 MeV, and (c) possible resonances at higher energies are compared to DWBA calculations for $\Delta L = 0$ (solid lines), 1 (dotted lines), and 2 (dashed lines). The results using the direct and sequential breakup backgrounds are denoted by the full circles and full squares, respectively. The previous results [37,38] are also added by the open circles. The vertical and horizontal bars denote the statistical errors and the size of angular bins, respectively.

the sequential breakup background (a factor of 2 for the direct breakup background), while that of $\Delta L = 2$ is more than 5. These results corroborate the 0^+ assignment to the excited state at 1.6 MeV.

It is interesting that the ground and second 0^+ states of ^{12}O carry a similar size of (p,t) cross sections. This is in contrast to ^{14}O , whose ground state has one order of magnitude larger cross sections than the 0_2^+ state in the $^{16}\text{O}(p,t)$ reaction at a proton energy of 54.1 MeV [56]. Assuming that the single-step $2n$ transfer process dominates, cross sections of $\Delta L = 0$ are governed by an overlap between the initial and final state wave functions, and are particularly sensitive to the fraction of the proton $(1p_{1/2})^2$ configuration in the final 0^+ state. Since $^{14,16}\text{O}$ are both magic nuclei with a marginal mixing of other intruder configurations in the ground state, the $^{16}\text{O}(p,t)$ reaction should favor the ground state of ^{14}O more than the 0_2^+ state, which supposedly has a much less $(1p_{1/2})^2$ configuration assuming the symmetry with the ^{14}C 0_2^+ state [57]. In the $^{14}\text{O}(p,t)$ reaction, in contrast, the disappearance of the shell closure at $Z = 8$ occurs in ^{12}O [37,38], making the $(1p_{1/2})^2$ component fragmented over the ground and second 0^+ states to a similar level [28]. This would result in more balanced cross sections from the ^{14}O ground state. A quantitative discussion requires further reaction analyses based on the coupled reaction channel formalism [58] and fine adjustments of optical potential model parameters using elastic scattering data.

Figure 8(c) shows the differential cross sections deduced from the Voigt functions at 4.2 and 7.0 MeV, respectively, that were obtained from the fits with the direct breakup background. Both angular distributions have a rather smooth and decreasing trend toward larger angles, and the diffractive patterns are not as clear as in the ground and 0_2^+ states. The cross sections for the 4.2-MeV data slightly rise at 45° , which is in line with the diffractive angle of $\Delta L = 1$. The differential cross sections largely match the DWBA calculation with $\Delta L = 1$ over the

angular domain of the measurement. The J^π would be 1^- if this resonance is true and singlet. The 7.0-MeV data have a shallow dip near 50° , which favors $\Delta L = 0$ over $\Delta L = 1$ and 2. The differential cross sections, however, deviate from the calculation at forward angles with no distinct peak at the predicted diffractive angle around 35° . The J^π of this possible resonance is hence not evident.

V. DISCUSSION

The 0_2^+ state of ^{12}O is compared to its mirror nucleus ^{12}Be [30] in Fig. 9. It is seen that the measured excitation energy of the ^{12}O 0_2^+ state is lower by 0.63 MeV than that of the ^{12}Be state. The absolute magnitude of the shift is comparable to a 0.67-MeV shift observed for the 0_2^+ states between ^{14}O and

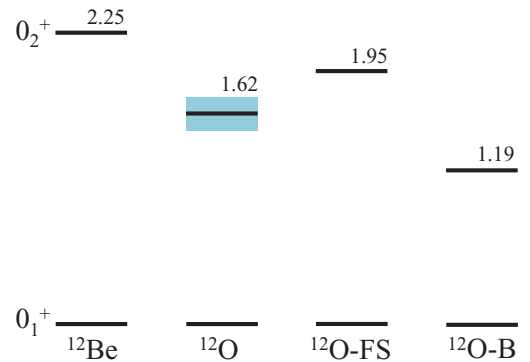


FIG. 9. Comparison of the 0_2^+ state of ^{12}O to the mirror state in ^{12}Be and theoretical predictions of ^{12}O [28]. The E_x values are given in MeV. The experimental error of the ^{12}O 0_2^+ state is denoted by the filled area. The statistical and systematic errors are added. The predictions labeled FS and B are based on the wave functions of Fortune and Sherr [28] and Barker [27], respectively.

^{14}C [59], while the present result should be considered to be a more significant Coulomb shift given the smaller Z for the ^{12}O and ^{12}Be pair. There are a few theoretical predictions on the 0_2^+ state of ^{12}O [27,28]. The predicted excitation energies are compared to the data in Fig. 9. While neither prediction perfectly reproduces the data, with Fortune and Sherr's E_x higher than the experimental value and Barker's much lower, both are compatible with the data in that the 0_2^+ state is lowered in ^{12}O with respect to ^{12}Be . The two predictions differ in the ratio of valence proton configurations, but they agree that the combined total of the $2s_{1/2}$ and $1p$ configurations amounts to nearly 90%. These orbitals lower the Coulomb energy more readily than other orbitals with higher angular momenta, as their binding energies are nearing zero. While the ground 0^+ state is also mixture of s and p configurations, these orbitals extend more in the 0_2^+ state due to its smaller binding energy. The reduced overlap with the Coulomb field of the core results in a lower Coulomb energy. This qualitatively accounts for the lowering of the excitation energy of the 0_2^+ state.

To further our understanding, we compare the mirror energy difference (MED) of the ^{12}O 0_2^+ state to known mirror 0^+ states as a function of binding energies. We expect that if the finite-size effects are manifested in the MED, it should introduce a binding energy dependence to the MED, which would otherwise be independent of binding energies. To establish systematics for nuclei with different sizes and charges, we normalize these effects by scaling MED and binding energies. Our MED and its scaling are based on the method proposed in Ref. [49], where even-odd nuclei are studied by the two-body model with one valence proton and a core. In this method, the proton (S_p) or neutron (S_n) emission thresholds are taken as the Fermi energy. The MED of partnering states is defined as the energy difference of the proton and neutron states relative to these thresholds, $\Delta E_{\text{MED}} = (E_x^p - S_p) - (E_x^n - S_n)$, where E_x^p and E_x^n denote the excitation energies of the proton- and neutron-rich states, respectively. The MED thus defined is scaled with a nominal Coulomb energy U carried by the valence proton. The resulting $\Delta E_{\text{MED}}/U$ ratio, or scaled MED, serves as an indicator of reduction or enhancement of MED. U is given by $6(Z-1)e^2/5R$, assuming a uniformly charged spherical core [49]. R denotes the two-body scaling length, for which the radius formula $1.27(A-1)^{1/3}$ fm was adopted in Ref. [49]. Here A denotes the mass number of the given nucleus.

In the case of 0^+ states, the two-body picture may not be appropriate as two nucleons in the same valence orbital equally contribute to the MED. To extend the aforementioned method to 0^+ states, we adopt the three-body picture in which two valence nucleons are coupled to a core. The MED for two nucleons is defined by replacing S_p and S_n with the two-proton (S_{2p}) and two-neutron (S_{2n}) separation energies, namely $\Delta E_{\text{MED}} = (E_x^p - S_{2p}) - (E_x^n - S_{2n})$. The reference length used for the scaling factor U is also modified. We adopt the hyperradius ρ_0 , a widely used length to measure the size of a three-body system. We use the definition that Riisager *et al.* used in Ref. [12] to scale the radii of $2n$ halo states:

$$\rho_0^2 = \sum_{i < k} \frac{m_i m_k}{m_{\text{unit}} m_{\text{tot}}} R_{ik}^2,$$

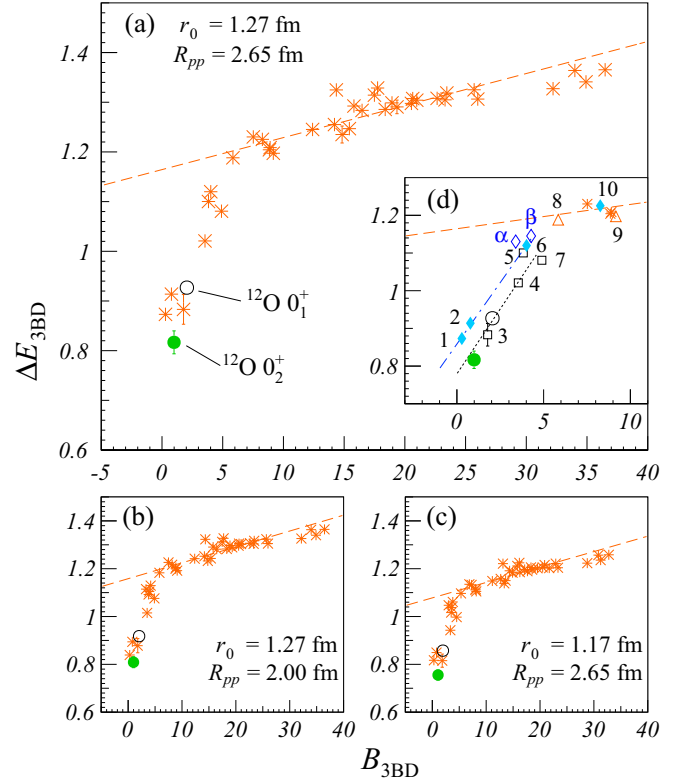


FIG. 10. $\Delta E_{3\text{BD}}$ vs $B_{3\text{BD}}$ plots for mirror 0^+ states. The data of the ground and second 0^+ states of ^{12}O are denoted by the open and filled circles, respectively. The plots with three different sets of r_0 and R_{pp} are shown in panels (a) to (c). Panel (d) magnifies an area with small $B_{3\text{BD}}$. For nuclei with $A \leq 18$, mirror states with substantial $2s_{1/2}$ and $1p$ components are denoted by the open squares and solid diamonds, respectively, while the other states are by open triangles. The data include (1) ^6Be - ^6He 0_1^+ , (2) ^8C - ^8He 0_1^+ , (3) ^{16}Ne - ^{16}C 0_2^+ , (4) ^{16}Ne - ^{16}C 0_1^+ , (5) ^{14}O - ^{14}C 0_2^+ , (6) ^{10}C - ^{10}Be 0_1^+ , (7) ^{18}Ne - ^{18}O 0_3^+ , (8) ^{18}Ne - ^{18}O 0_2^+ , (9) ^{18}Ne - ^{18}O 0_1^+ , and (10) ^{14}O - ^{14}C 0_1^+ . The labels α and β denote *ab initio* NCSM calculations [21] for the ^{10}C - ^{10}Be 0_1^+ pair using the AV8' interaction [76] and the AV8' + TM'(99) interaction [77], respectively. The dotted and dash-dotted lines are to guide the eyes.

where the constituent particles are labeled by the indices $i, k = 0$ to 2. R_{ik} denotes the two-body scaling length between the i th and k th particles. m_i is the mass of the i th particle with $m_{\text{tot}} = m_0 + m_1 + m_2$. m_{unit} is the so-called unit mass that will also be used for the scaling factor of the binding energies. For the three-body model with $2p$ and the core, the hyperradius reads

$$\rho_0^2 = 2 \frac{A-2}{A} R_{cp}^2 + \frac{1}{A} R_{pp}^2,$$

where R_{cp} denotes the two-body scaling length between the core and a proton and R_{pp} that of the two protons. Here we use the proton mass for m_{unit} . We adopt $R_{cp} = r_0(A-2)^{1/3}$ with $r_0 = 1.27$ fm [49] and $R_{pp} = 2.65$ fm [50]. The choice of these values will be examined later. The scaling factor for two protons is defined as $U_{3\text{BD}} = 12(Z-2)e^2/5\rho_0$. The scaled MED will be referred to as $\Delta E_{3\text{BD}} = \Delta E_{\text{MED}}/U_{3\text{BD}}$ hereafter.

TABLE I. Experimental data and deduced quantities of the mirror 0^+ states adopted for the $\Delta E_{3\text{BD}}$ vs $B_{3\text{BD}}$ plots in Fig. 10. The proton- and neutron-rich nuclei of a given mirror pair are listed in the columns of ${}^A Z_p$ and ${}^A Z_n$, respectively. The S_{2p} and S_{2n} values all are adopted from the latest compilation [26]. The errors are given in parentheses only when the rounded values are greater than zero.

${}^A Z_p$	${}^A Z_n$	ρ_0 (fm)	S_{2p} (MeV)	S_{2n} (MeV)	E_x^p (MeV)	E_x^n (MeV)	B (MeV)	$B_{3\text{BD}}$	ΔE_{MED} (MeV)	$\Delta E_{3\text{BD}}$
${}^6\text{Be}$	${}^6\text{He}$	2.57	-1.37(1)	0.98	0	0	0.87(1)	0.29	2.35(1)	0.87
${}^8\text{C}$	${}^8\text{He}$	2.98	-2.11(2)	2.13	0	0	1.75(2)	0.78(1)	4.24(2)	0.91
${}^{10}\text{C}$	${}^{10}\text{Be}$	3.32	3.82	8.48	0	0	7.29	4.02	4.66	1.12
${}^{12}\text{O}$	${}^{12}\text{Be}$	3.61	-1.64(2)	3.67	0	0	3.14(2)	2.05(2)	5.31(2)	0.93
					1.62(13) ^a	2.25 [30]	1.52(13)	0.99(9)	4.68(13)	0.82(2)
${}^{14}\text{O}$	${}^{14}\text{C}$	3.87	6.57	13.12	0	0	11.03	8.27	6.55	1.23
					5.92(1) [59]	6.59 [59]	5.11(1)	3.83(1)	5.88(1)	1.10
${}^{16}\text{Ne}$	${}^{16}\text{C}$	4.10	-1.40(2)	5.47	0	0	4.21(2)	3.54(2)	6.87(2)	1.02
					2.10(20) [68]	3.03 [60,67]	2.11(20)	1.77(17)	5.94(20)	0.88(3)
${}^{18}\text{Ne}$	${}^{18}\text{O}$	4.31	4.52	12.19	0	0	9.86	9.17	7.67	1.20
					3.58 [69]	3.63 [69]	6.28	5.84	7.61	1.19
					4.59(1) [63]	5.34 [69]	5.27(1)	4.90(1)	6.92(1)	1.08
${}^{20}\text{Mg}$	${}^{20}\text{O}$	4.50	2.34(3)	11.56	0	0	8.72(3)	8.85(3)	9.23(3)	1.20
${}^{22}\text{Mg}$	${}^{22}\text{Ne}$	4.68	7.94	17.13	0	0	14.08	15.43	9.19	1.25
					5.95 [70]	6.24 [70]	8.12	8.90	8.91	1.21
					7.22 [70]	7.34 [70]	6.86	7.52	9.07	1.23
${}^{24}\text{Si}$	${}^{24}\text{Ne}$	4.85	3.43(2)	14.07	0	0	10.55(2)	12.40(2)	10.64(2)	1.25
${}^{26}\text{Si}$	${}^{26}\text{Mg}$	5.00	7.79	18.42	0	0	14.68	18.38	10.64	1.29
					3.34 [71]	3.59 [71]	11.34	14.20	10.39	1.26
${}^{28}\text{S}$	${}^{28}\text{Mg}$	5.15	3.36(16)	14.95	0	0	11.18(16)	14.83(21)	11.58(16)	1.24(2)
${}^{30}\text{S}$	${}^{30}\text{Si}$	5.29	7.14	19.08	0	0	14.75	20.65	11.94	1.31
${}^{32}\text{Ar}$	${}^{32}\text{Si}$	5.42	2.72	15.79	0	0	11.20	16.48	13.07	1.28
${}^{34}\text{Ar}$	${}^{34}\text{S}$	5.55	6.94	20.06	0	0	15.23	23.46	13.12	1.32
					3.87 [72]	3.92 [72]	11.36	17.49	13.07	1.31
					4.97 [72]	5.23 [72]	10.26	15.81(1)	12.86	1.29
					5.91(1) [72]	5.85 [72]	9.32(1)	14.36(2)	13.18(1)	1.32
${}^{36}\text{Ca}$	${}^{36}\text{S}$	5.67	2.65(4)	16.88	0	0	11.78(4)	18.94(6)	14.22(4)	1.30
${}^{38}\text{Ca}$	${}^{38}\text{Ar}$	5.79	6.40	20.63	0	0	15.35	25.71	14.22	1.33
					3.08 [73]	3.38 [73]	12.26	20.54	13.93	1.30
					4.75 [73]	4.71 [73]	10.60(1)	17.75(1)	14.26(1)	1.33
${}^{40}\text{Ti}$	${}^{40}\text{Ar}$	5.90	1.37(16)	16.47	0	0	11.12(16)	19.35(28)	15.10(16)	1.29(1)
${}^{42}\text{Ti}$	${}^{42}\text{Ca}$	6.01	4.84	19.84	0	0	14.41	26.00	15.01	1.31
					1.85 [74]	1.84 [74]	12.56	22.66	15.02	1.31
${}^{46}\text{Cr}$	${}^{46}\text{Ti}$	6.21	6.50(2)	22.72	0	0	16.69(2)	32.20(4)	16.22(2)	1.33
${}^{48}\text{Ni}$	${}^{48}\text{Ca}$	6.31	-1.31(5)	17.23	0	0	10.54(5)	20.98(10)	18.54(5)	1.30
${}^{50}\text{Fe}$	${}^{50}\text{Cr}$	6.41	6.24(6)	23.58(1)	0	0	17.02(6)	34.92(12)	17.34(6)	1.34
${}^{54}\text{Zn}$	${}^{54}\text{Cr}$	6.59	-1.48(2)	17.66	0	0	10.74(2)	23.31(4)	19.14(2)	1.30
${}^{54}\text{Ni}$	${}^{54}\text{Fe}$	6.59	5.47(5)	24.06(1)	0	0	16.82(5)	36.49(11)	18.60(5)	1.37
${}^{58}\text{Zn}$	${}^{58}\text{Ni}$	6.76	2.97(5)	22.46	0	0	14.88(5)	34.00(11)	19.49(5)	1.36

^aPresent work. The statistical and systematic errors are added in parentheses.

The binding energy of two protons is defined as $B = S_{2p} + 2(Z-2)e^2/\rho_0 - E_x^p$. The second term is meant to take the Coulomb barrier into account using ρ_0 . The dimensionless binding energy is given by Riisager's scaling method [12], $B_{3\text{BD}} = m_{\text{unit}} B \rho_0^2 / \hbar^2$.

The $\Delta E_{3\text{BD}}$ vs $B_{3\text{BD}}$ plot for mirror 0^+ states with $A = 6$ to 58 is shown in Fig. 10(a). Detailed properties of these states are summarized in Table I. The plot reveals remarkably well-defined correlations between $\Delta E_{3\text{BD}}$ and $B_{3\text{BD}}$, indicating the validity of the scaling relation to represent MED and binding energies. The plot is roughly divided into two regions above and below $B_{3\text{BD}} \sim 5$. The former region with larger binding energies is characterized by a shallow slope of gradually

decreasing $\Delta E_{3\text{BD}}$. The correlation is nearly linear and most of the data fall within $\pm 5\%$ around the best fit line shown by the dashed line. This linear correlation, however, breaks near $B_{3\text{BD}} = 5$. As $B_{3\text{BD}}$ nears zero, $\Delta E_{3\text{BD}}$ follows a much steeper slope and drops to as low as 60% of the deeply bound data. The ${}^{12}\text{O}$ 0_2^+ state, denoted by the solid circle, has one of the smallest values of $B_{3\text{BD}}$. The downward shift of 0.63 MeV for the 0_2^+ state (Fig. 9) corresponds to 11% of the nominal Coulomb energy $U = 5.7$ MeV. The deduced $\Delta E_{3\text{BD}}$ of 0.82 is thus lower by 0.11 compared to that (0.93) obtained for the ground 0^+ state (open circle), marking the lowest among the data. This lowering is clearly in line with the overall trend of other weakly bound states. While the choice of parameters

r_0 and R_{pp} is arbitrary to certain degree, these trends are essentially the same within a reasonable level of changes as shown in Fig. 10(b) with $R_{pp} = 2.0$ fm and Fig. 10(c) with $r_0 = 1.17$ fm.

Weakly bound 0^+ states are thus characterized by the drastic lowering of $\Delta E_{3\text{BD}}$. To understand its origin, mirror states with substantial $2s_{1/2}$ [57,60–63] and $1p$ components [64–66] are denoted in Fig. 10(d). The other states are either governed by higher L components or deeply-bound. It is seen that the states with lower $\Delta E_{3\text{BD}}$ with respect to the dashed line mostly involve these components carrying small angular momenta of $L = 0$ or 1. These components increasingly lose Coulomb energies as $B_{3\text{BD}}$ gets smaller, which makes $\Delta E_{3\text{BD}}$ sharply decline. The gradual evolution of $\Delta E_{3\text{BD}}$ in the deeply bound states above $B_{3\text{BD}} = 5$ indicates that the Coulomb energy lowers its sensitivity to binding energies and angular momenta. The small $\Delta E_{3\text{BD}}$ value of the ^{12}O 0_2^+ state in turn supports the theoretical studies predicting $1p$ and $2s_{1/2}$ configurations for the valence protons [27,28]. While not conclusive from the limited data, the degree of decrease slightly differs between $L = 0$ and 1 in Fig. 10(d). $\Delta E_{3\text{BD}}$ of the $2s_{1/2}$ states (dotted line) is lowered more than that of the $1p$ states (dot-dashed line). This is similar to radii of $L = 0$ neutrons, which show a sharper rise than other L due to the absence of the centrifugal barrier as shown in the calculations of Ref. [75]. The data of both ground and 0_2^+ state of ^{12}O are in line with the slope of $L = 0$, suggesting substantial mixing of the $2s_{1/2}$ component. This agrees with the mirror states in ^{12}Be , in which mixing of the $2s_{1/2}$ component has been noticed [29–31,33].

It is surprising that such a strict scaling relation of dimensionless $\Delta E_{3\text{BD}}$ and $B_{3\text{BD}}$ universally marks the asymmetry of weakly bound states with various masses. We conclude this discussion by pointing out two possible impacts of this finding. First, the scaling relation of $\Delta E_{3\text{BD}}$ and $B_{3\text{BD}}$ provides a reference to assess to what degree finite binding effects are reproduced in theoretical calculations, almost independently of other effects that influence level energies. It will hence be interesting to see if large-scale shell model or *ab initio* calculations reproduce this scaling relation. While calculations of separation energies for a pair of mirror 0^+ states are generally lacking, there is one previous *ab initio* no-core shell model (NCSM) calculation that provides a set of ground state energies of ^{10}C , ^{10}Be , and their common core ^8Be [21]. The $\Delta E_{3\text{BD}}$ and $B_{3\text{BD}}$ values were deduced from the predictions made using effective interactions derived from the Argonne V8' (AV8') potential [76] with and without the chiral-symmetry based Tucson-Melbourne TM'(99) three-nucleon interaction [77] [β and α in Fig. 10(d), respectively]. While relying on a limited number of harmonic-oscillator bases, both NCSM results with and without the TM'(99) interaction well reproduce the experimental data of the ^{10}C - ^{10}Be 0_1^+ state, which is down by about 5% to the dashed line and thus indicates a slightly lowered MED. Comparison to future calculations of more unstable mirror nuclei will be interesting.

Another aspect is more related to general properties of low-energy quantum systems. Scaling relations are often thought to be related to universality [12]. Universal phenomena loosely depend on the details of interactions at short distances and thus

emerge in various systems at different scales under certain scaling relations. One such example of this long-standing subject in quantum physics is the Efimov three-body state governed by the s -wave scattering length [78]. Debated for nuclear states such as triton, the ^{12}C Hoyle state [78], or $2n$ halo states [8,10,79], the first Efimov state has recently been discovered in ultracold atomic gases [80–82]. The work of Ref. [12] points out that the size and binding energy of halo states fulfill a universal scaling rule, which provides a general classification of such states in physics. It is shown that the scaling relation obtained from a few-body model using Woods-Saxon and Gaussian potentials [83] explains experimental data of nuclear halo states as well as theoretical results from Faddeev calculations of other systems such as the ^4He trimer using realistic potentials of the van der Waals force [84]. It will be interesting to investigate if the scaling of MED is also related to universal aspects of atomic nuclei that have yet to be revealed.

VI. SUMMARY

To study the level scheme of unbound ^{12}O , we remeasured the $^{14}\text{O}(p,t)$ reaction at 51 MeV/u using a radioactive beam provided by the LISE fragment separator of GANIL. Statistics were improved by almost one order of magnitude higher than the previous study [37,38]. Recoiling tritons off the cryogenic hydrogen target were detected by an array of MUST2 telescopes. The excitation energy of ^{12}O and the scattering angle of the reaction were deduced by the missing mass method using the energy and angle of recoiling tritons. A resonance was clearly identified near 1.6 MeV in the resulting excitation energy spectrum. The predicted doublet of a 0^+ and 2^+ state near this energy was carefully dealt with. It was concluded from the angular dependence of the resonance yields that a 0^+ state constitutes the major contribution of the observed resonance. The excitation energy and the natural width of the 0^+ state were deduced to be $1.62 \pm 0.03(\text{stat.}) \pm 0.10(\text{syst.})$ MeV and $1.2 \pm 0.1(\text{stat.})_{-0.7}^{+0.3}(\text{syst.})$ MeV, respectively, from the data of $\theta_{\text{c.m.}} = 25^\circ$ to 45° , where the yields of the 0^+ resonance concentrate. The differential cross sections deduced were well reproduced by DWBA calculations with $\Delta L = 0$, thus confirming the 0^+ assignment. The energies and widths of the resonance were found to shift outside $\theta_{\text{c.m.}} = 25^\circ$ to 45° , still suggesting a minor contribution of a 2^+ state. As the possibility that these shifts originate in experimental uncertainties cannot be ruled out, more precise measurements are desirable to conclude or exclude this possible doublet. While other resonances were suggested at 4.2 and 7.0 MeV, they are contingent on the assumption of the direct breakup background.

The excitation energy of the 0_2^+ state in ^{12}O is by 0.63 MeV lower than the mirror state in neutron-rich ^{12}Be . This sizable downward shift was discussed in comparison with systematics of other known 0^+ states. To establish the systematics, we introduced a dimensionless mirror energy difference $\Delta E_{3\text{BD}}$ and binding energy $B_{3\text{BD}}$ to normalize the effects of size and charge of nuclei. The $\Delta E_{3\text{BD}}$ vs $B_{3\text{BD}}$ plot indicates a sharp scaling relation between the mirror energy difference and binding energy that is met by various nuclei with different sizes. Weakly bound 0^+ states with $L = 0$ or 1 valence

nucleons are characterized by lower $\Delta E_{3\text{BD}}$ values compared to deeply bound states, which is qualitatively explained by the same mechanism of the Thomas-Ehrman shift. The $\Delta E_{3\text{BD}}$ of the $^{12}\text{O } 0_2^+$ state is one of the lowest among the known mirror 0^+ states, indicating predominant $2s_{1/2}$ or $1p$ configurations for the valence protons as predicted by previous theoretical works [27,28]. The scaling relation of mirror asymmetry is expected to provide a good test for structural calculations in the proximity of the drip lines and to help explore universality inherent in atomic nuclei.

ACKNOWLEDGMENTS

We thank the technical staff members of GANIL for their professional work. This work was supported by the European Community FP6 “Structuring the ERA - Integrated Infrastructure Initiative,” contract EURONS No. RII3-CT-2004-506065. We thank Emmanuel Rindel of the IPN Orsay for making the schematic drawing of the experimental setup for this paper. D.S. thanks Shumpei Endo of Ecole Normale Supérieure for fruitful discussions and the Japan Society for the Promotion of Science for support.

-
- [1] I. Tanihata, H. Hamagaki, O. Hashimoto, Y. Shida, N. Yoshikawa, K. Sugimoto, O. Yamakawa, T. Kobayashi, and N. Takahashi, *Phys. Rev. Lett.* **55**, 2676 (1985).
- [2] P. G. Hansen and B. Jonson, *Europhys. Lett.* **4**, 409 (1987).
- [3] J. Dobaczewski, W. Nazarewicz, T. R. Werner, J. F. Berger, C. R. Chinn, and J. Dechargé, *Phys. Rev. C* **53**, 2809 (1996).
- [4] I. Stefan, F. de Oliveira Santos, O. Sorlin, T. Davinson, M. Lewitowicz, G. Dumitru, J. C. Angélique, M. Angélique, E. Berthoumieux, C. Borcea, R. Borcea, A. Buta, J. M. Daugas, F. de Grancey, M. Fadil, S. Grevy, J. Kiener, A. Lefebvre-Schuhl, M. Lenhardt, J. Mrazek, F. Negoita, D. Pantelica, M. G. Pellegriti, L. Perrot, M. Płoszajczak, O. Roig, M. G. Saint-Laurent, I. Ray, M. Stanoiu, C. Stodel, V. Tatischeff, and J. C. Thomas, *Phys. Rev. C* **90**, 014307 (2014).
- [5] M. V. Zhukov, B. V. Danilin, D. V. Fedorov, J. M. Bang, I. J. Thomson, and J. S. Vaagen, *Phys. Rep.* **231**, 151 (1993).
- [6] K. Hagino and H. Sagawa, *Phys. Rev. C* **72**, 044321 (2005).
- [7] T. Nakamura, A. M. Vinodkumar, T. Sugimoto, N. Aoi, H. Baba, D. Bazin, N. Fukuda, T. Gomi, H. Hasegawa, N. Imai, M. Ishihara, T. Kobayashi, Y. Kondo, T. Kubo, M. Miura, T. Motobayashi, H. Otsu, A. Saito, H. Sakurai, S. Shimoura, K. Watanabe, Y. X. Watanabe, T. Yakushiji, Y. Yanagisawa, and K. Yoneda, *Phys. Rev. Lett.* **96**, 252502 (2006).
- [8] D. V. Fedorov, A. S. Jensen, and K. Riisager, *Phys. Rev. Lett.* **73**, 2817 (1994).
- [9] A. S. Jensen, K. Riisager, D. V. Fedorov, and E. Carrido, *Rev. Mod. Phys.* **76**, 215 (2004).
- [10] D. L. Canham and H.-W. Hammer, *Euro. Phys. J. A* **37**, 367 (2008).
- [11] E. Braaten and H.-W. Hammer, *Phys. Rep.* **428**, 259 (2006).
- [12] K. Riisager, D. V. Fedorov, and A. S. Jensen, *Eur. Phys. Lett.* **49**, 547 (2000).
- [13] C. R. Hoffman, B. P. Kay, and J. P. Schiffer, *Phys. Rev. C* **89**, 061305(R) (2014).
- [14] H. Sagawa and K. Hagino, *Eur. Phys. J. A* **51**, 102 (2015).
- [15] N. Michel, W. Nazarewicz, M. Płoszajczak, and K. Bennaceur, *Phys. Rev. Lett.* **89**, 042502 (2002).
- [16] C. Yuan, C. Qi, F. Xu, T. Suzuki, and T. Otsuka, *Phys. Rev. C* **89**, 044327 (2014).
- [17] G. Hagen, T. Papenbrock, and M. Hjorth-Jensen, *Phys. Rev. Lett.* **104**, 182501 (2010).
- [18] T. Otsuka, M. Honma, T. Mizusaki, N. Shimizu, and Y. Utsuno, *Prog. Part. Nucl. Phys.* **47**, 319 (2001).
- [19] B. A. Brown, *Prog. Part. Nucl. Phys.* **47**, 517 (2001).
- [20] R. B. Wiringa, S. C. Pieper, J. Carlson, and V. R. Pandharipande, *Phys. Rev. C* **62**, 014001 (2000).
- [21] P. Navrátil and W. E. Ormand, *Phys. Rev. C* **68**, 034305 (2003).
- [22] S. C. Pieper, R. B. Wiringa, and J. Carlson, *Phys. Rev. C* **70**, 054325 (2004).
- [23] P. Navrátil, S. Quaglioni, I. Stetcu, and B. R. Barrett, *J. Phys. G* **36**, 083101 (2009).
- [24] J. B. Ehrman, *Phys. Rev.* **81**, 412 (1951).
- [25] R. G. Thomas, *Phys. Rev.* **88**, 1109 (1952).
- [26] M. Wang, G. Audi, A. H. Wapstra, F. G. Kondev, M. MacCormick, X. Xu, and B. Pfeiffer, *Chin. Phys. C* **36**, 1603 (2012).
- [27] F. C. Barker, *Phys. Rev. C* **59**, 535 (1999).
- [28] H. T. Fortune and R. Sherr, *Phys. Rev. C* **82**, 034325 (2010).
- [29] S. Shimoura *et al.*, *Phys. Lett. B* **560**, 31 (2003).
- [30] S. Shimoura *et al.*, *Phys. Lett. B* **654**, 87 (2007).
- [31] R. Meharchand, R. G. T. Zegers, B. A. Brown, S. M. Austin, T. Baugher, D. Bazin, J. Deaven, A. Gade, G. F. Grinyer, C. J. Guess, M. E. Howard, H. Iwasaki, S. McDaniel, K. Meierbachtol, G. Perdikakis, J. Pereira, A. M. Prinke, A. Ratkiewicz, A. Signoracci, S. Stroberg, L. Valdez, P. Voss, K. A. Walsh, D. Weisshaar, and R. Winkler, *Phys. Rev. Lett.* **108**, 122501 (2012).
- [32] H. Iwasaki *et al.*, *Phys. Lett. B* **491**, 8 (2000).
- [33] A. Navin, D. W. Anthony, T. Aumann, T. Baumann, D. Bazin, Y. Blumenfeld, B. A. Brown, T. Glasmacher, P. G. Hansen, R. W. Ibbotson, P. A. Lofy, V. Maddalena, K. Miller, T. Nakamura, B. V. Pritychenko, B. M. Sherrill, E. Spears, M. Steiner, J. A. Tostevin, J. Yurkon, and A. Wagner, *Phys. Rev. Lett.* **85**, 266 (2000).
- [34] G. J. KeKelis, M. S. Zisman, D. K. Scott, R. Jahn, D. J. Vieira, J. Cerny, and F. Ajzenberg-Selove, *Phys. Rev. C* **17**, 1929 (1978).
- [35] S. Mordechai, P. A. Seidl, C. F. Moore, L. C. Bland, R. Gilman, K. S. Dhuga, H. T. Fortune, C. L. Morris, and S. J. Greene, *Phys. Rev. C* **32**, 999 (1985).
- [36] R. A. Kryger, A. Azhari, M. Hellstrom, J. H. Kelley, T. Kubo, R. Pfaff, E. Ramakrishnan, B. M. Sherrill, M. Thoennessen, S. Yokoyama, R. J. Charity, J. Dempsey, A. Kirov, N. Robertson, D. G. Sarantites, L. G. Sobotka, and J. A. Winger, *Phys. Rev. Lett.* **74**, 860 (1995).
- [37] D. Suzuki, H. Iwasaki, D. Beaumel, L. Nalpas, E. Pollacco, M. Assie, H. Baba, Y. Blumenfeld, N. DeSereville, A. Drouart, S. Franchoo, A. Gillibert, J. Guillot, F. Hammache, N. Keeley, V. Lapoux, F. Marechal, S. Michimasa, X. Mougeot, I. Mukha, H. Okamura, H. Otsu, A. Ramus, P. Roussel-Chomaz, H. Sakurai, J. A. Scarpaci, O. Sorlin, I. Stefan, and M. Takechi, *Phys. Rev. Lett.* **103**, 152503 (2009).
- [38] D. Suzuki, *Eur. Phys. J. A* **48**, 130 (2012).

- [39] M. F. Jager, R. J. Charity, J. M. Elson, J. Manfredi, M. H. Mahzoon, L. G. Sobotka, M. McCleskey, R. G. Pizzone, B. T. Roeder, A. Spiridon, E. Simmons, L. Trache, and M. Kurokawa, *Phys. Rev. C* **86**, 011304(R) (2012).
- [40] E. Pollacco *et al.*, *Eur. Phys. J. A* **25**, 287 (2005).
- [41] R. Anne and A. C. Mueller, *Nucl. Instrum. Methods B* **70**, 276 (1992).
- [42] P. Dolégiéviez, A. Gillibert, W. Mittig, X. Mougeot, A. Obertelli, F. de Oliveira, M. Ozille, Ph. Robillard, P. Roussel-Chomaz, and H. Savajols, *Nucl. Instrum. Methods Phys. Res., Sect. A* **564**, 32 (2006).
- [43] S. Ottini-Hustache *et al.*, *Nucl. Instrum. Methods Phys. Res., Sect. A* **431**, 476 (1999).
- [44] P. Baron *et al.*, *Nucl. Science Symp. Record. IEEE* **1**, 386 (2003).
- [45] J. F. Ziegler *et al.*, *Nucl. Instrum. Methods Phys. Res., Sect. B* **268**, 1818 (2010).
- [46] S. Agostinelli *et al.* (GEANT4 Collaboration), *Nucl. Instrum. Methods Phys. Res., Sect. A* **506**, 250 (2003).
- [47] W. Voigt, *Sitzungsber. K. Bayer. Akad. Wiss.* **42**, 603 (1912).
- [48] F. Ajzenberg-Selove and J. H. Kelley, *Nucl. Phys. A* **506**, 1 (1990).
- [49] A. Muta and T. Otsuka, *Prog. Theor. Phys. Suppl.* **142**, 355 (2001).
- [50] D. V. Fedorov, A. S. Jensen, and K. Riisager, *Phys. Rev. C* **49**, 201 (1994).
- [51] I. J. Thompson, in *Fifty Years of BCS: Pairing in Finite Systems*, edited by R. A. Broglia and V. Zelevinsky (World Scientific, Singapore, 2013), p. 455.
- [52] B. F. Bayman and A. Kallio, *Phys. Rev.* **156**, 1121 (1967).
- [53] I. J. Thompson, *Comput. Phys. Rep.* **7**, 167 (1988).
- [54] A. J. Koning and J. P. Delaroche, *Nucl. Phys. A* **713**, 231 (2003).
- [55] F. D. Becchetti, Jr. and G. W. Greenlees, in *Polarization Phenomena in Nuclear Reactions* (The University of Wisconsin Press, Madison, 1971), p. 682.
- [56] D. G. Fleming, J. C. Hardy, and J. Cerny, *Nucl. Phys. A* **162**, 225 (1971).
- [57] S. Mordechai, H. T. Fortune, G. E. Moore, M. E. Cobern, R. V. Kollarits, and R. Middleton, *Nucl. Phys. A* **301**, 463 (1978).
- [58] N. Keeley *et al.*, *Phys. Lett. B* **646**, 222 (2007).
- [59] F. Ajzenberg-Selove, *Nucl. Phys. A* **523**, 1 (1991).
- [60] A. H. Wuosmaa, B. B. Back, S. Baker, B. A. Brown, C. M. Deibel, P. Fallon, C. R. Hoffman, B. P. Kay, H. Y. Lee, J. C. Lighthall, A. O. Macchiavelli, S. T. Marley, R. C. Pardo, K. E. Rehm, J. P. Schiffer, D. V. Shetty, and M. Wiedeking, *Phys. Rev. Lett.* **105**, 132501 (2010).
- [61] H. T. Fortune and S. C. Headley, *Phys. Lett. B* **51**, 136 (1974).
- [62] R. D. Lawson, F. J. D. Serduke, and H. T. Fortune, *Phys. Rev. C* **14**, 1245 (1976).
- [63] A. V. Nero, E. G. Adelberger, and F. S. Dietrich, *Phys. Rev. C* **24**, 1864 (1981).
- [64] T. Oishi, K. Hagino, and H. Sagawa, *Phys. Rev. C* **90**, 034303 (2014).
- [65] T. Myo and K. Katō, *Prog. Theor. Exp. Phys.* (2014) 083D01.
- [66] Y. Kanada-En'yo and H. Horiuchi, *Phys. Rev. C* **68**, 014319 (2003).
- [67] H. T. Fortune, R. Middleton, M. E. Cobern, G. E. Moore, S. Mordechai, R. V. Kollarits, H. Nann, W. Chung, and B. H. Wildenthal, *Phys. Lett. B* **70**, 408 (1977).
- [68] K. Fohl, R. Bilger, H. Clement, J. Grater, R. Meier, J. Patzold, D. Schapler, G. J. Wagner, O. Wilhelm, W. Kluge, R. Wieser, M. Schepkin, R. Abela, F. Foroughi, and D. Renker, *Phys. Rev. Lett.* **79**, 3849 (1997).
- [69] D. R. Tilley, H. R. Weller, C. M. Cheves, and R. M. Chasteler, *Nucl. Phys. A* **595**, 1 (1995).
- [70] M. Shamsuzzoha Basunia, *Nucl. Data Sheets* **127**, 69 (2015).
- [71] P. M. Endt, *Nucl. Phys. A* **633**, 1 (1998).
- [72] N. Nica and B. Singh, *Nucl. Data Sheets* **113**, 1563 (2012).
- [73] J. A. Cameron and B. Singh, *Nucl. Data Sheets* **109**, 1 (2008).
- [74] B. Singh and J. A. Cameron, *Nucl. Data Sheets* **92**, 1 (2001).
- [75] K. Riisager, A. S. Jensen, and P. Møller, *Nucl. Phys. A* **548**, 393 (1992).
- [76] B. S. Pudliner, V. R. Pandharipande, J. Carlson, S. C. Pieper, and R. B. Wiringa, *Phys. Rev. C* **56**, 1720 (1997).
- [77] S. A. Coon and H. K. Han, *Few-Body Syst.* **30**, 131 (2001).
- [78] V. Efimov, *Phys. Lett. B* **33**, 563 (1970).
- [79] B. Acharya, C. Ji, and D. R. Phillips, *Phys. Lett. B* **723**, 196 (2013).
- [80] M. Zaccanti, B. Deissler, C. D'Errico, M. Fattori, M. Jona-Lasinio, S. Müller, G. Roati, M. Inguscio, and G. Modugno, *Nat. Phys.* **5**, 586 (2009).
- [81] N. Gross, Z. Shotan, S. Kokkelmans, and L. Khaykovich, *Phys. Rev. Lett.* **103**, 163202 (2009).
- [82] S. E. Pollack, D. Dries, and R. G. Hulet, *Science* **326**, 1683 (2009).
- [83] D. V. Fedorov, A. S. Jensen, and K. Riisager, *Phys. Lett. B* **312**, 1 (1993).
- [84] E. Nielsen, D. V. Fedorov, and A. S. Jensen, *J. Phys. B* **31**, 4085 (1998).